PCCP

Tuning the oxygen electrocatalysis via strain on LaNiO3(001)

Tuning the oxygen electrocatalysis via strain on LaNiO$_3$(001)[+]

Simuck F. Yuk and Valentino R. Cooper*

Materials Science and Technology Division, Oak Ridge National Laboratory, Oak Ridge, TN 37831, USA

Abstract

The slow kinetics of the oxygen evolution (OER) and oxygen reduction (ORR) reactions hamper the development of renewable energy storage and conversion technologies. Transition-metal oxides (TMOs) are cost-effective replacements to conventional noble metal catalysts for driving these electrochemical systems. Strain is known to greatly affect the electronic structure of TMO surfaces, leading to significant changes in their electrocatalytic activities. In this study, we explore the influence of strain on the OER and ORR mechanisms on the $LaNiO_3(001)$ surface using density functional theory (DFT). Through a comparison of the overpotential and the largest change in Gibbs free energy (ΔG) in the reaction pathway, we determined that OER activity on the $LaNiO_3$ surface is directly related to the desorption of -H from the surface, which can be tuned as a function of strain. Moreover, tensile strain shuts off the reaction pathway to forming the $-O_2H$ intermediate state, due to the dissociation of $-O_2H$ into $-O_2$ and $-H$. This is largely a consequence of the strong binding of H to the surface O, leading to a significant increase in the largest ΔG for the ORR on the tensile-strained surfaces by promoting an alternative reaction pathway. Overall, our results show that tensile strain on $LaNiO_3(001)$ leads to a decrease in both OER and ORR activities. Interestingly, in both cases, we find that the reaction is driven by the interactions with surface O ions, thus calling for a reinterpretation of the role that Ni e_g orbital polarization plays in defining the OER and ORR catalytic activity on the TMO surfaces. Here, it is an indirect measure of changes in Ni-O hybridization, which controls the binding of -H species to the surface. As such, these results highlight the importance of surface O ions; particularly as it relates to defining molecule-surface interactions that ultimately tune and enhance the electrocatalytic efficiency of perovskite materials through the modulation of strains.

Keywords: electrocatalysis, strain, perovskite oxides, density functional theory, surface thermodynamics

I. Introduction

The development of renewable energy storage and conversion technologies, such as metal-air batteries, fuel cells, and water-splitting devices, requires a better understanding of two key electrochemical reactions, the oxygen evolution reaction (OER) and oxygen reduction reaction (ORR).[1-7] Electrocatalysts involving precious metals such as Pt, RuO_2 or IrO_2 are routinely used to facilitate either the OER or ORR activities at room temperature.[8-12] However, even in the presence of such catalysts, the kinetics of OER/ORR are often sluggish, limiting the performance and commercialization of promising electrochemical energy applications.[13, 14] Therefore, substantial efforts have been focused on creating more effective oxygen electrocatalysts and elucidating the underlying mechanisms of OER/ORR. Bifunctionality, by which the catalyst is capable of promoting both the OER and ORR under different reaction conditions, is also a desirable aim since using a single bifunctional oxygen electrode would increase the mobility of charge carriers or simplify the design of energy storage systems.[6, 7, 15]

Transition-metal oxides (TMO) are cost-effective alternatives to noble metal materials, with different combinations of metal cations and oxide structures available for unique catalyst designs.[16-18] Under compressive epitaxial strain, $LaNiO_3$ (LNO) is one of the most promising, perovskite-based, TMO catalyst candidates; recently demonstrating bifunctional activity comparable to that of the best-performing precious metals.[19] In particular, the σ^* orbital (e_g) occupancy of perovskite oxides is correlated with the ORR and OER activities due to strong overlap between the O $2p_\sigma$ and the B-cation e_g states, which are particularly sensitive to the strain state of the surface.[16, 17] In this case, the e_g band polarization (i.e. difference in orbital populations of d_{z^2} and $d_{x^2-y^2}$ states) has been proposed as the key descriptor of the overall trend in catalytic behavior on strained LNO(001) films. Applying epitaxial strain induces splitting of e_g orbitals, which leads to the polarization of surface d_{z^2} and $d_{x^2-y^2}$ states, which has been correlated to both the OER and ORR activities.[20-23] Thus, strain-induced changes in electronic structure present an effective route for tuning catalytic performance.[19, 23-29]

In this study, we investigated the role that epitaxial strain plays in altering the formation of adsorbed intermediates that control the OER/ORR catalytic reactivity of an ABO_3-based electrocatalysts. To elucidate these fundamental mechanisms, we employed density functional theory (DFT) calculations to study the strain-induced changes in the surface-bound configurations of –H, –H_2O, –OH, –O, –O_2, and –O_2H on LNO(001). Both the OER and ORR are known to proceed via these intermediate states on the oxide surfaces, transferring four electrons in the process.[16, 17, 30-34] A total of 7 different strain states (-3%, -2%, -1%, 0%, +1%, +2%, and +3% relative to the unstrained LNO surface) were systematically examined. The adsorption energy of these surface-bound intermediate states changes greatly with strain, where the most variation in energy is observed via applying tensile strain. We found that both the overpotential and largest change in Gibbs free energy (ΔG) for OER are directly related to the adsorption strength of –H, which can be modified as a function of strain. Most surprisingly, the presence of tensile strain shuts off the reaction pathway to forming the –O_2H state, significantly altering the ORR mechanism and its largest ΔG on LNO(001). In both cases, the strong binding of -H to surface oxygen ions suggests that the conventional picture of dependence on e_g orbital polarization can be recast as a measure of changes in Ni-O hybridization which controls the adsorption of -H to the surface. These strain-induced changes in surface thermodynamics present a route to tuning and enhancing the electrocatalytic efficiency of perovskite materials.

II. Computational Details

All DFT calculations were performed with the *Vienna Ab initio Simulation Package* (VASP)[35-37] using projector augmented wave (PAW) potentials. We used a plane-wave energy cutoff of 500 eV with a Gaussian smearing width of 0.2 eV (increasing the energy cutoff to 600 eV leads to negligible changes in adsorption energies (<~0.001 eV/molecule)). The Perdew-Burke-Erzenhoff (PBE)[38] form of the generalized gradient approximation (GGA) was employed to describe exchange and correlation effects. We chose a Hubbard U value of 4 eV for the Ni d-states for all calculations – this correctly reproduced the experimental X-ray linear dichroism (XLD) pattern as demonstrated in Ref. 19. A periodic (2×2) LNO(001) asymmetric slab, consisting of 5 LaO and 5 NiO_2 layers, was considered to maintain charge neutrality. A Monkhorst-Pack[39] k-point mesh of $6 \times 6 \times 1$ was applied for our DFT slab calculations. The relevant chemical species were

4

subsequently adsorbed on the NiO_2-terminated LNO(001) surface. The NiO_2 termination was chosen for our slab model to closely match the experimentally relevant termination.[19] The BFGS algorithm[40] was used to relax the atoms with a force criterion of 0.01 eV/Å. All the atoms were fully optimized while the in-plane axis was fixed for each strain state.

The optimized lattice parameters (a = 5.419 Å and c = 13.010 Å), obtained from bulk LNO (R3cH) calculations using an $8 \times 8 \times 2$ k-point mesh, were set for our unstrained slab structures. This is in good agreement with the experimental values of a = 5.457 Å and c = 13.146 Å.[41] To remove any spurious interactions between the top and bottom of the slab, we used a vacuum region of at least 18 Å. The adsorption energy of surface-bound –H, –H_2O, –OH, –O, –O_2, and –O_2H intermediate states, ΔE_{ads}, is defined by $\Delta E_{ads} = E_{ads-surf} - E_{bare-surf} - E_{gas}$, where $E_{ads-surf}$ and $E_{bare-surf}$ are the energy of adsorbate-covered and bare $LaNiO_3$ surfaces, respectively. E_{gas} is the energy of the isolated adsorbate molecule. We have excluded the translational, rotational, vibrational, and configurational entropy contributions since the sum of these contributions was determined to be relatively small when calculating the Gibbs free energy (please refer to Sec. 1.2 of the Supporting Information for additional details).

III. Results and Discussion

ΔE_{ads} (eV/molecule)			
Type	-3%	0%	+3%
-H	-2.090	-2.144	-2.168
-H_2O	-0.528	-0.735	-1.012
-O_2	0.027	0.073	-0.018
-OH	-2.074	-2.030	-2.187
-O	1.472	1.552	0.940
-O_2H	-1.048	-0.997	Disso.
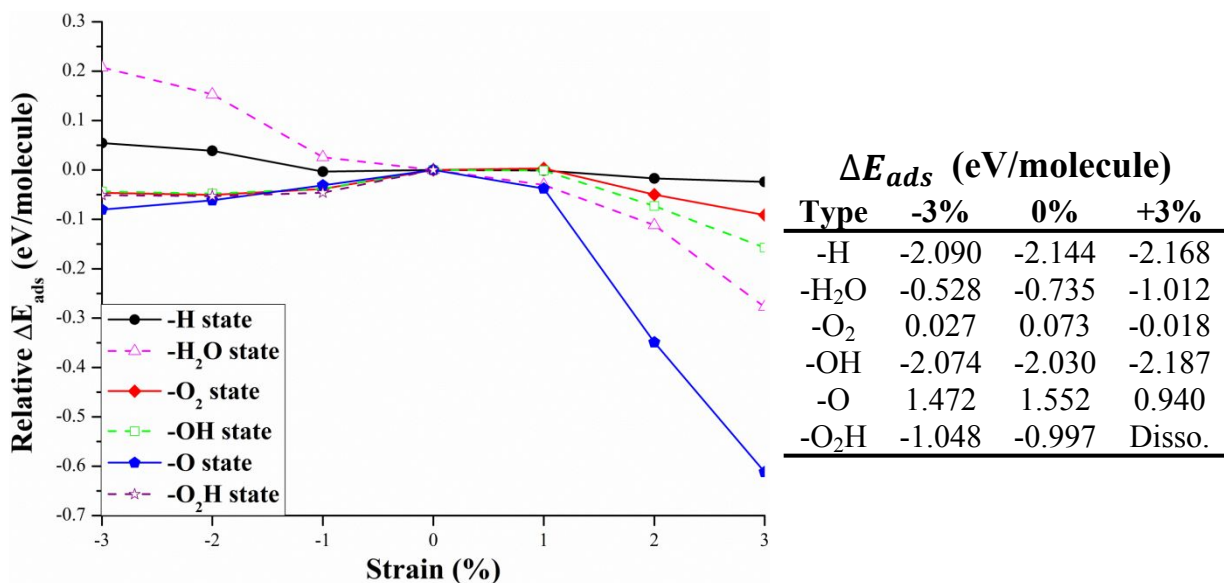
Figure 1. ΔE_{ads} of surface-bound –H, –H_2O, –O_2, –OH, –O, and –O_2H species relative to the unstrained state as a function of strain (please refer to Table S3 and Table S4 for the magnitude

of ΔE_{ads}). The absolute magnitude of ΔE_{ads} at -3%, 0%, and +3% is also displayed for each species.

As a first step towards understanding the strain-induced changes in the electrocatalytic mechanism on the LNO surface, we examined the adsorption energetics of –H_2O, –OH, –O, –O_2, and –O_2H species on the top site of surface Ni, along with –H on the top site of surface O as a function of strain (the initial and DFT-optimized configurations can be found in Sec. 1.1 of the Supporting Information). The overall trend of ΔE_{ads} (relative to the unstrained state) for these configurations on the LNO(001) can be seen in Fig. 1. In the case of compressive strain, we observe only modest changes in the binding energy of all molecules to the LNO(001) surface. On the other hand, tensile strain causes a significant increase in the binding strength of molecules to the LNO(001) surface, with the adsorption of –O being most pronounced. Most interestingly, we could not stabilize -O_2H on the tensile-strained LNO(001) surface; i.e. –O_2H dissociates into –O_2 and –H, as shown in Fig. 2a. (Note: To confirm the dissociation of –O_2H, we used the relaxed configuration of –O_2H from the unstrained surface and attempted to re-adsorb it as an initial structure on the tensile-strained LNO surfaces in multiple orientations.) Such strain-dependent –O_2H behavior hints that the OER and ORR mechanisms are significantly modified with the introduction of different strain states.
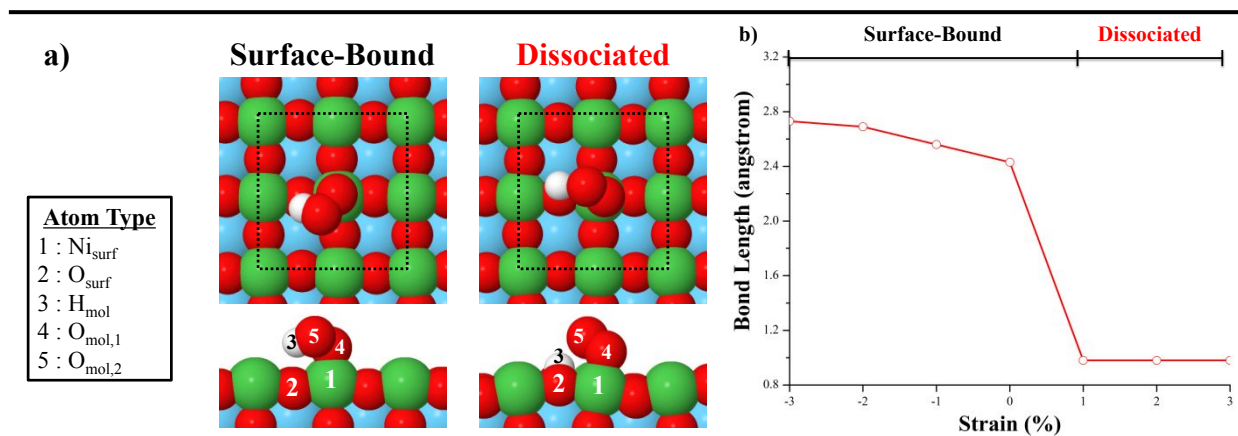
Figure 2. a) DFT-optimized geometry of surface bound and dissociated O_2H on the LNO(001) surface and b) the change in bond distance between the surface O (O_{surf}) and the hydrogen atom of the O_2H molecule (H_{mol}) as a function of strain (Please refer to Table S1 for the full details on the bond lengths and angles of adsorbed O_2H).

To understand the dissociation of $-O_2H$ on the tensile-strained surfaces, we examined the changes in the adsorption geometry of $-O_2H$ on the LNO(001) surface induced by the variation in strains. A significant change in bond length between the surface O (O_{surf}) and the hydrogen atom of the O_2H molecule (H_{mol}) can be seen as a function of strain (see Fig. 2b). As the distance between the surface atoms (O_{surf}-Ni_{surf}) increase when going from the compressive to the unstrained state, the bond length between O_{surf} and H_{mol} decreases, indicating that the H_{mol} is gradually pulled towards the O_{surf} with increasing strain. A strong preference of H towards the surface O over Ni can be confirmed by ΔE_{ads} of H on the LNO(001) as shown in Figure 2b and Table S4. Also, the decrease in bond angle between the surface atoms and molecular oxygen (O_{surf} -Ni_{surf}-$O_{mol,1}$) indicates that the O_2H molecule leans towards the surface as the strain increases, as shown in Table S1. After the dissociation of $-O_2H$ into $-H$ and $-O_2$ for tensile strains, no significant change in the adsorbate geometries is seen with any of the dissociated species. We also did not observe any major change within the $-O_2H$ molecular geometry prior to its dissociation, as evidenced by the negligible change in the $O_{mol,1}$-$O_{mol,2}$ and $O_{mol,2}$-H_{mol} bond distances and the H_{mol}-$O_{mol,2}$-$O_{mol,1}$ bond angle (summarized in Table S1). Thus, the dissociation of $-O_2H$ occurs mainly due to the strong interaction of H atom with the surface O, resulting in a detachment from the molecular O_2 when the bond length of surface O-Ni is sufficiently large.

The instability of $-O_2H$ on the LNO(001) surface implies that both the OER and ORR reactions would proceed along an alternative reaction pathway than the previously reported four-electron-transfer mechanisms.[16, 17, 30-34] Since the interaction between H and the surface O is strong on the LNO surface, the adsorption/desorption step of H on the surface O also needs to be considered when formulating the reaction pathway. In addition, we also included the adsorption/desorption step of H_2O on the surface Ni. After such modification, we searched for the particular OER pathway which yields the lowest theoretical overpotential amongst the possible mechanisms. Table 1 shows two possible pathways for the reversible OER/ORR, modified from the OER mechanism originally proposed by Man and co-workers.[33] In the following section, we analyze the effects of these alternative pathways on the reaction thermodynamics in order to get a better understanding of how strain controls the overall OER and ORR mechanism on the LNO surface.

7

Table 1. Reversible OER/ORR pathways on the LNO(001) modified from the OER mechanism originally proposed by Man and co-workers.[33] Please refer to Sec. 1.4 of the Supporting Information for the definition of ΔG for each reaction step.

Reaction Pathway #1 (With –O₂H)		Reaction Pathway #2 (Without –O₂H)	
$H_2O(l) + \ast \leftrightarrow H_2O^\ast$	(1)	$H_2O(l) + \ast \leftrightarrow H_2O^\ast$	(1)
$H_2O^\ast + \ast \leftrightarrow OH^\ast + H^\ast$	(2)	$H_2O^\ast + \ast \leftrightarrow OH^\ast + H^\ast$	(2)
$OH^\ast + H^\ast \leftrightarrow OH^\ast + \ast + (H^+ + e^-)$	(3)	$OH^\ast + H^\ast \leftrightarrow OH^\ast + \ast + (H^+ + e^-)$	(3)
$OH^\ast + \ast + H_2O(l) \leftrightarrow OH^\ast + H_2O^\ast$	(4)	$OH^\ast + \ast + H_2O(l) \leftrightarrow OH^\ast + H_2O^\ast$	(4)
$OH^\ast + H_2O^\ast + \ast \leftrightarrow 2OH^\ast + H^\ast$	(5)	$OH^\ast + H_2O^\ast + \ast \leftrightarrow 2OH^\ast + H^\ast$	(5)
$2OH^\ast + H^\ast \leftrightarrow 2OH^\ast + \ast + (H^+ + e^-$	(6)	$2OH^\ast + H^\ast \leftrightarrow 2OH^\ast + \ast + (H^+ + e^-)$	(6)
$2OH^\ast \leftrightarrow O_2H^\ast + H^\ast$	(7)	$2OH^\ast + \ast \leftrightarrow O_2^\ast + 2H^\ast$	(7)
$O_2H^\ast + H^\ast \leftrightarrow O_2H^\ast + \ast + (H^+ + e^-)$	(8)	$O_2^\ast + 2H^\ast \leftrightarrow O_2^\ast + H^\ast + \ast + (H^+ + e^-$	(8)
$O_2H^\ast + \ast \leftrightarrow O_2^\ast + H^\ast$	(9)	$O_2^\ast + H^\ast \leftrightarrow 2\ast + O_2 + (H^+ + e^-)$	(9)
$O_2^\ast + H^\ast \leftrightarrow 2\ast + O_2 + (H^+ + e^-)$	(10)		

We first determine the theoretical overpotential of OER (η_{OER}) by adopting the computational Standard Hydrogen Electrode (SHE) approach.[31-33, 42-46] The detailed derivation of this model is shown in Sec. 1.3 of the Supporting Information. η_{OER} is independent of both the pH or the potential (ΔV) since the change in Gibbs free energy (ΔG) of each step will be varied in similar ways with pH and ΔV. Thus, ΔG and η_{OER} are calculated under standard conditions ($T = $ 298.15 K, $pH = 0$) with $\Delta V = 0$ (the definition of ΔG for each reaction step is summarized in Sec. 1.4 of the Supporting Information). The effect of the solvent was also neglected in this study since 1) the SHE model already accounts H_2O as a reference[42] and 2) the interaction of H_2O with the surface-bound intermediates is relatively small due to the steric effects between H_2O and the surface oxygen atoms present on the oxidized surfaces.[32, 33] One of the most important parameters that can be deduced from the SHE model is the potential-determining step, which is the step with the largest ΔG in the OER pathway ($\Delta G^{OER} = \max \ [\Delta G]$). As the potential increases, this step will be the last to move downhill in the OER energy diagram. The magnitude of this step can then be

used to calculate η_{theor} for a particular reaction pathway ($\eta_{OER} = (\frac{\Delta G^{OER}}{e}) - 1.23\ V$), allowing us to estimate the catalytic reactivity of OER on the LNO(001) surface. Ultimately, this model can provide critical insights into the overall thermodynamic trends along the reaction paths.
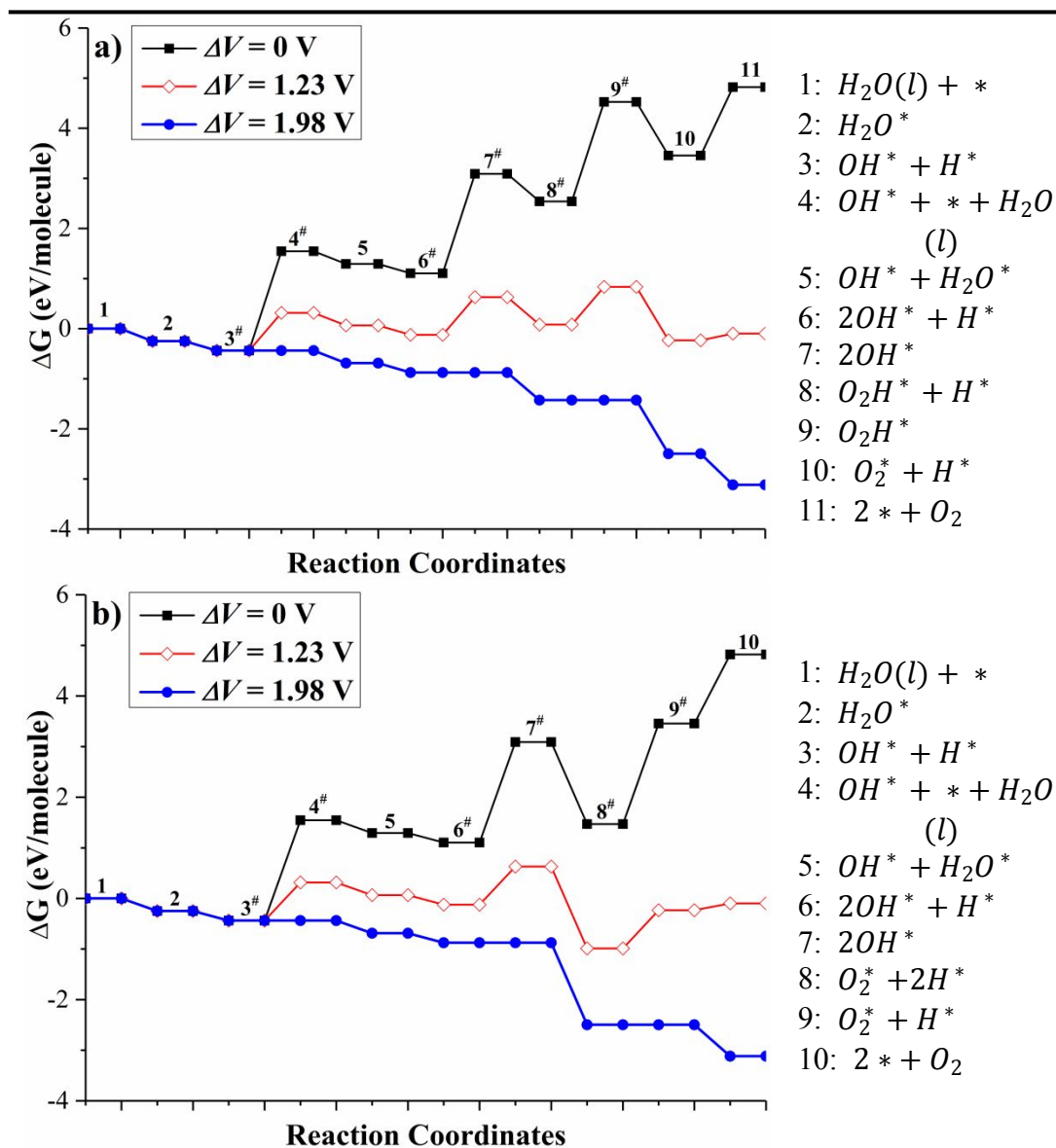
Figure 3. Gibbs free energy diagram of OER pathway a) #1 and b) #2 on the unstrained LNO(001) surface at $\Delta V = 0$ V (black solid squares), 1.23 V (red open diamonds) and 1.98 V (blue solid circles). The potential-determining steps are marked with # sign. Please refer to Fig. S4 of the Supporting Information for Gibbs free energy diagram of OER pathway as a function of strain.

Fig. 3 summarizes the Gibbs free energy diagram for OER pathway #1 and #2 (based on Table 1) while varying ΔV on the unstrained LNO(001) surface. At $\Delta V = 0$ V, many of the steps remain energetically uphill, including the ones that involve the desorption of H on the surface O. As ΔV increases to 1.23 V, we can see that some of these steps now move downhill. Finally, at ΔV = 1.98 V, all the steps, including the potential-determining step, become energetically downhill, indicating that η_{OER} = 1.98 − 1.23 = 0.75 V for both reaction pathway #1 and #2. Interestingly, Tkalych and co-workers have also reported their η_{OER} to be between 0.62 and 0.75 V for the associative, single-site OER mechanism on the stoichiometric and fully-hydroxylated β-NiOOH(001) surface.[34] A similar trend in ΔG can be found with other strains states, but resulting in different values of η_{OER} due to the variation in binding strength of intermediate species on the strained LNO surfaces. Again, unlike for the compressive-strained/unstrained states, the tensile-strained states can only occur via reaction pathway #2 due to the dissociation of –O$_2$H. However, it is important to note that the potential-determining step for both reaction pathways #1 and #2 involves H desorption from the LNO surface (step 3 to 4, 6 to 7, and 8 to 9; $H^* \leftrightarrow * + (H^+ + e^-$)). Since the ΔE_{ads} of H is enhanced for tensile-strains (see Fig. 1), more energy will be required to desorb H from the surface O. Fig. 4 presents the overall trend in η_{OER} as a function of strain, showing the lowest value of overpotential for the -3% strained state where η_{OER} = 0.70 V and higher value of η_{OER} on the tensile-strained surfaces (η_{OER} = 2.00 − 1.23 = 0.77 V at +3% strained state). These findings are in good qualitative agreement with the trends in OER activity of strained LNO(001) surfaces reported from the recent experimental study.[19]

10
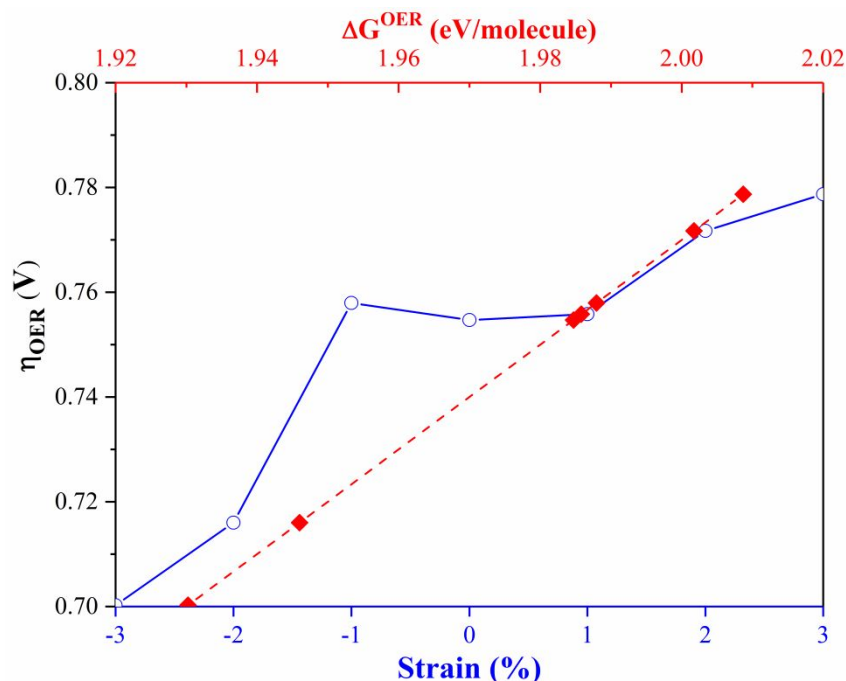
Figure 4. η_{OER} for the reaction pathway #1 and #2 as a function of strain (open blue circles) and ΔG^{OER} (closed red squares) for the OER on the LNO(001) surface. Refer to Table S5 for the magnitude of ΔG^{OER} and η_{OER}.

In order to investigate the electronic structure origins of OER activity on strained LNO, we also examined the change in density of states (DOS) for the surface O as a function of strain states since it is directly associated with the OER potential-determining step (desorption of H). Particularly, the position of the band center was determined as a function for different strain states and compared against η_{OER} since it has been regarded as a good indicator for describing the adsorbate-surface bond strength.[47-55] In fact, we found a clear linear correlation between η_{OER} and the band center of O p_z orbital (see Fig. 5a). Such relationship reveals that the band center of the O p_z can be considered as a descriptor for the OER activity on the strained LNO(001). Also, the change in adjacent Ni d-valence orbitals, especially e_g, can be related to the reactivity of LNO, as already reported in previous literature for various types of oxide surfaces.[20-23] For the OER on the LNO(001) surface, we expect that the strain-induced change in H bonding on the surface O atom drives the shift in e_g orbitals of adjacent Ni atom. Again, we observed a strong correlation between η_{OER} and the band center of Ni e_g measured after the adsorption of H on the surface O (see Fig. 5b). Thus, the shift in electronic structures, induced by surface strain, is closely related to the

11

change in the OER activity. Overall, these findings confirm the importance of surface O atom, showing that the trend observed with surface Ni e_g on the LNO(001) is mainly induced by the change in H bonding to the surface O atom as a function of strain.
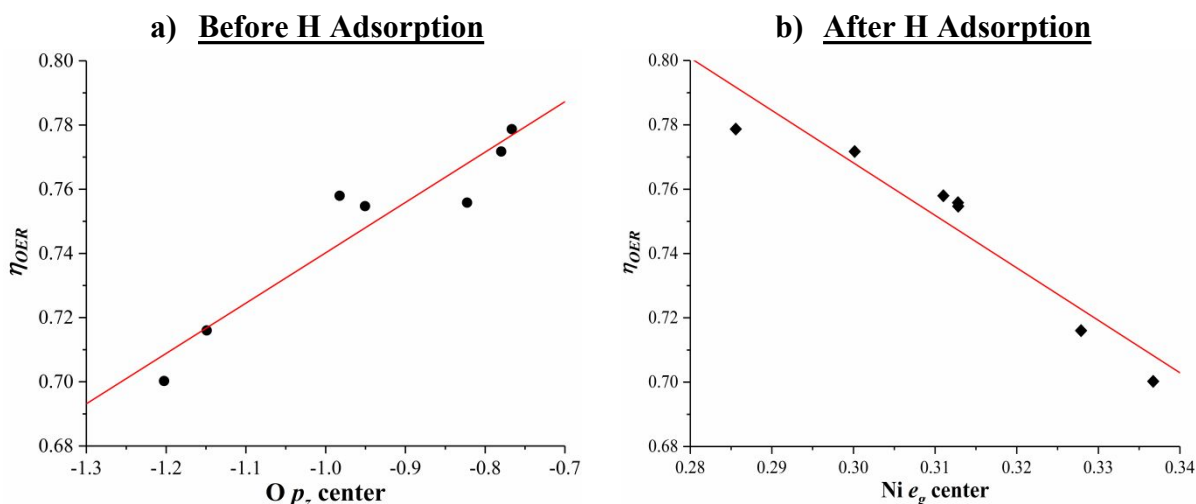
Figure 5. Band center of a) surface O p_z on the bare LNO(001) and b) surface Ni e_g after H adsorption on the surface O vs. OER theoretical overpotential (η_{OER}) for various strain states. Note that the band center of O p_z and Ni e_g were measured after excluding the strongly hybridized Ni 3d – O 2p states below approximately -4 to -3 eV relative to Fermi level (comparable to the d-band center in metals).[19] Refer to Table S6 for the magnitude of band centers and corresponding η_{OER}.

Fig. 6 depicts the Gibbs free energy diagram for the ORR pathway #1 and #2 on the unstrained LNO(001) surface at $\Delta V = 0$ V. Here, the SHE approach cannot be employed to measure the ORR theoretical overpotentials as some energetically uphill steps (such as step 2 to 3-1 or step 9 to 10 in Fig. 6) at $\Delta V = 0$ V are no longer potential-dependent, unlike in the OER pathway (see Sec. 1.4 of the Supporting Information for details). In short, these steps will stay energetically uphill regardless of the value of ΔV, thus limiting the ability to directly apply the SHE approach. However, (as seen in Fig. 4) there is a linear relationship between η_{OER} and the reaction step with the largest ΔG of the OER pathways, ΔG^{OER}. In this regard, the preferred reaction coordinate can also be defined by the ORR pathway (#1 or #2) which yields the lowest ΔG^{ORR}. Therefore, we can approximate the strain dependence of the ORR activity by computing ΔG^{ORR} as a function of strain. It is interesting to note that the only difference between the ORR pathway #1 and #2 is the

location of the largest ΔG: $O_2^* + H^* \rightarrow O_2H^* + *$ (step 2 to 3-1) for reaction pathway #1 and

$O_2^* + 2H^* \rightarrow 2OH^* + *$ (step 3-3 to 4) for reaction pathway #2. In fact, ΔG^{ORR} is significantly

lower in reaction pathway #1 (unstrained and compressively strained surfaces) compared to

reaction pathway #2 (tensile-strained surfaces) (see Fig. 7). These strain-dependent trends in η_{OER}

and ΔG^{ORR} agree qualitatively with the previously-mentioned experimental study on

electrocatalytic activity of strained LNO(001) where the highest degree of bifunctional potential

was reached under compressive strains ($\sim$-1.2%).[19] In other words, tensile strains activate

alternative reaction pathways, thereby lowering the overall LNO(001) surface reactivity. A

significant increase in ΔG^{ORR} also qualitatively matches with the much lower and relatively flat

ORR reactivity observed in previous experimental studies on the strained LNO (001) surface.[19]
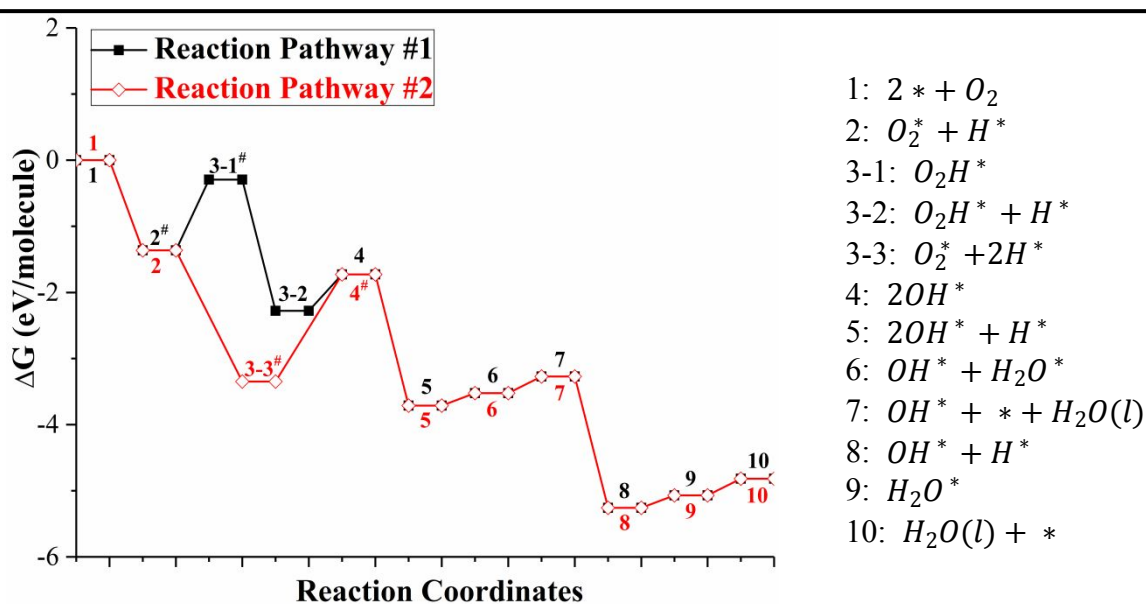
Figure 6. Gibbs free energy diagram of ORR pathway #1 and #2 on the unstrained LNO(001) surface at $\Delta V = 0$ V. The steps with largest ΔG are marked with # sign.

1: $2* + O_2$
2: $O_2^* + H^*$
3-1: O_2H^*
3-2: $O_2H^* + H^*$
3-3: $O_2^* + 2H^*$
4: $2OH^*$
5: $2OH^* + H^*$
6: $OH^* + H_2O^*$
7: $OH^* + * + H_2O(l)$
8: $OH^* + H^*$
9: H_2O^*
10: $H_2O(l) + *$
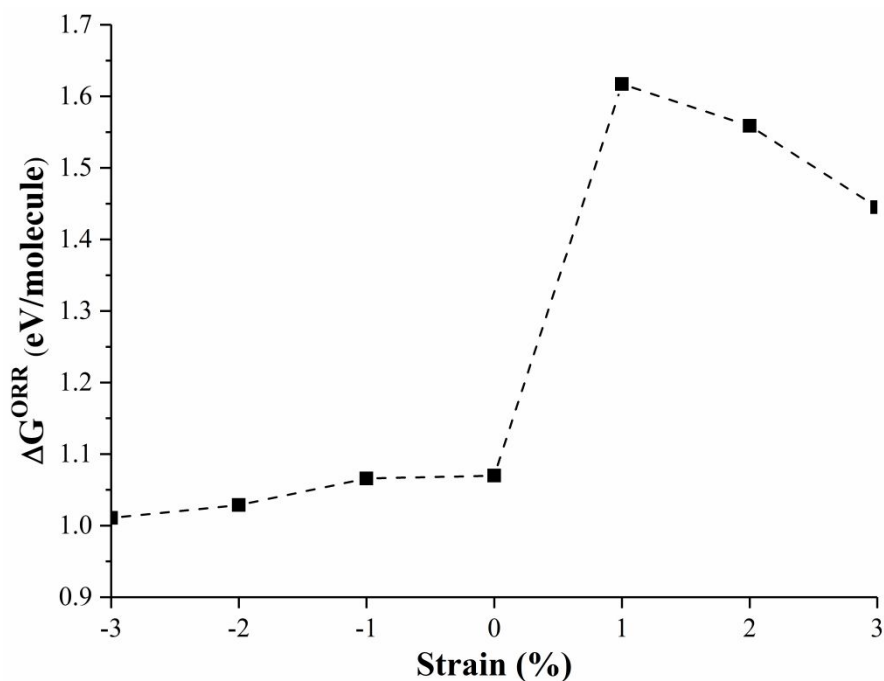
Figure 7. Overall trend in ΔG^{ORR} as a function of strain on the LNO(001) surface. Please refer to Table S5 for the magnitude of the ΔG^{ORR}.

Lastly, we also measured the formation energies of surface defects (O and Ni vacancies) with -2, 0 and +2 % strains to examine the possible effects of defect formation on the LNO(001) surface. For Ni vacancies, we discovered very large (thermodynamically unfavorable) vacancy formation energies of ~3.5 eV throughout the strain states. For O vacancies, vacancy formation energies of 0.553, 0.255 and 0.006 eV were found for the strain states of -2, 0 and +2 %, respectively. The resultant defect concentrations of surface O vacancies, as a function of temperature, is summarized in Fig. 8. Indeed, we find that, for large tensile strains, it may be possible to stabilize O vacancies on the surface. However, an inspection on the subsequent adsorption of OH to replace the missing O indicated that these vacancies would be quickly replaced by hydroxylated groups since OH adsorption energies (on the O vacancy site) were shown to be -3.463, -3.203, and -2.971 eV for -2, 0 and +2 % strains, respectively. Since the important step in the OER/ORR process involves the hydroxylated surface, and this would be a strongly thermodynamic surface, the process of removing an O atom for the strained LNO(001) surfaces would have no consequence for the predicted thermodynamic pathways.

14
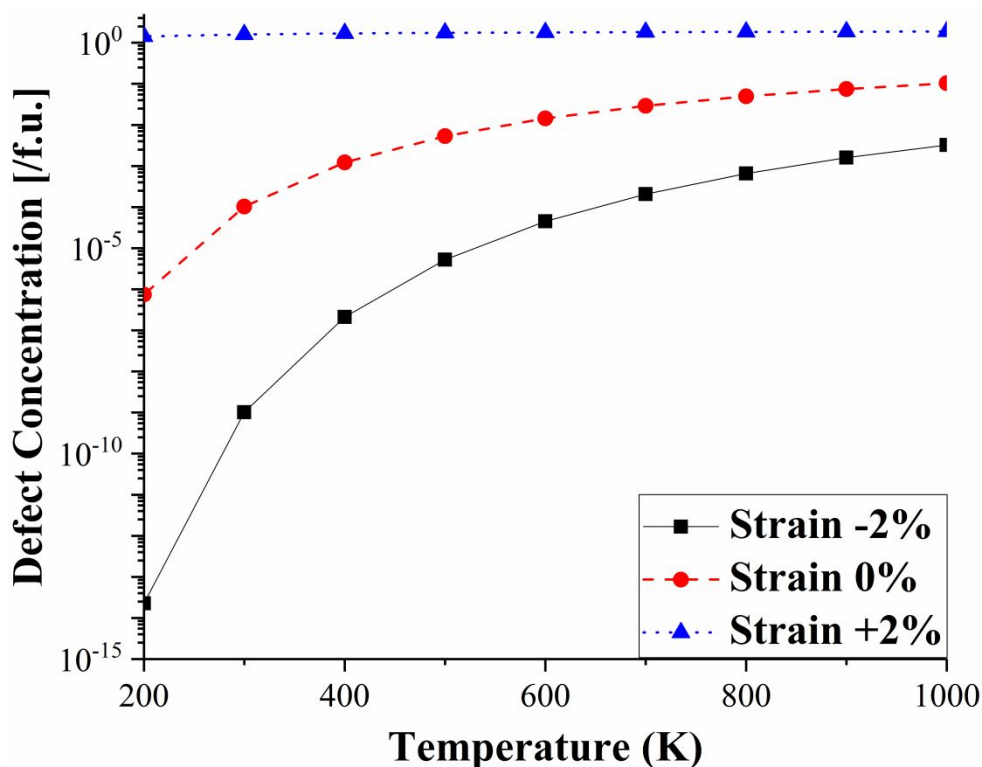
Figure 8. Defect concentration profile of surface O vacancy at -2, 0 and +2 % strained states as a function of temperature on the strained LNO(001).

IV. Conclusions

In conclusion, we have explored how strain influences the thermodynamics of the OER and ORR pathways; thereby tuning the overall electrocatalytic activity on the LNO(001) surface. Applying tensile strains blocks the formation of $-O_2H$ intermediate states and, as a result, activates an alternative reaction pathway. The dissociation of $-O_2H$ is caused by the strong binding of H on the surface O, which leads to its detachment from the molecular O_2 when the surface Ni-O bond length is sufficiently large. The inability to form $-O_2H$ intermediates leads to a significant increase in the largest ΔG for ORR on the tensile-strained surface which potentially leads to the decrease in reaction rate for ORR. This result explains both the lower and relatively flat ORR reactivity observed experimentally for strained LNO surfaces.

On the other hand, the OER overpotential is directly influenced by the desorption strength of H. The enhancement in adsorption energy of H under tensile strain leads to an increase in overpotential compared to the compressive and unstrained states. Strain significantly affects the surface Ni-O hybridization, which is reflected in the surface Ni e_g orbital polarization. Thus, such

15

hydrogen-driven activity implies that the universal trend of e_g seen with the OER and ORR on the oxide surfaces is an indirect effect of the changes of H bonding to the surface O. Overall, our study shows that it is possible to tune and enhance the electrocatalytic activity of perovskite materials via strain engineering which drives alternative reaction pathways and decreases the overpotential.

■ **Author Information**

Corresponding Author

Valentino R. Cooper
Senior R. & D. Staff Member
Oak Ridge National Laboratory
1 Bethel Valley Rd.
P.O. Box 2008 MS-6114
Bldg.: 4100, Rm: B375
Ph: (865) 574-5164

*E-mail: coopervr@ornl.gov.

■ **Conflicts of Interest**

There are no conflicts of interest to declare.

■ **Acknowledgment**

■ **References**

(1) Chen, G.; Bare, S. R.; Mallouk, T. E. *J. Electrochem. Soc.* **2002**, *149*, A1092-A1099.
(2) Lewis, N. S.; Nocera, D. G. *Proc. Natl. Acad. Sci. USA* **2006**, *103*, 15729-15735.
(3) Gray, H. B. *Nat. Chem.* **2009**, *1*, 7.
(4) Watanabe, M.; Tryk, D. A.; Wakisaka, M.; Yano, H.; Uchida, H. *Electrochim. Acta* **2012**, *84*, 187-201.
(5) Ge, X.; Sumboja, A.; Wuu, D.; An, T.; Li, B.; Goh, F. T.; Hor, T. A.; Zong, Y.; Liu, Z. *ACS*

Catal. **2015**, *5*, 4643-4667.

(6) Cheng, F.; Chen, J. *Chem. Soc. Rev.* **2012**, *41*, 2172-2192.

(7) Neburchilov, V.; Wang, H.; Martin, J. J.; Qu, W. *J. Power Sources* **2010**, *195*, 1271-1291.

(8) Trasatti, S. *Electrochim. Acta* **1984**, *29*, 1503-1512.

(9) Gasteiger, H. A.; Kocha, S. S.; Sompalli, B.; Wagner, F. T. *Appl. Catal., B* **2005**, *56*, 9-35.

(10) Greeley, J.; Stephens, I.; Bondarenko, A.; Johansson, T. P.; Hansen, H. A.; Jaramillo, T.; Rossmeisl, J.; Chorkendorff, I.; Nørskov, J. K. *Nat. Chem.* **2009**, *1*, 552-556.

(11) Lu, Y.-C.; Xu, Z.; Gasteiger, H. A.; Chen, S.; Hamad-Schifferli, K.; Shao-Horn, Y. *J. Am. Chem. Soc.* **2010**, *132*, 12170-12171.

(12) Lee, Y.; Suntivich, J.; May, K. J.; Perry, E. E.; Shao-Horn, Y. *J. Phys. Chem. Lett.* **2012**, *3*, 399-404.

(13) Katsounaros, I.; Cherevko, S.; Zeradjanin, A. R.; Mayrhofer, K. J. *Angew. Chem. Int. Ed.* **2014**, *53*, 102-121.

(14) Hong, W. T.; Risch, M.; Stoerzinger, K. A.; Grimaud, A.; Suntivich, J.; Shao-Horn, Y. *Energy Environ. Sci.* **2015**, *8*, 1404-1427.

(15) Zhigang, S.; Baolian, Y.; Ming, H. *J. Power Sources* **1999**, *79*, 82-85.

(16) Suntivich, J.; Gasteiger, H. A.; Yabuuchi, N.; Nakanishi, H.; Goodenough, J. B.; Shao-Horn, Y. *Nat. Chem.* **2011**, *3*, 546-550.

(17) Suntivich, J.; May, K. J.; Gasteiger, H. A.; Goodenough, J. B.; Shao-Horn, Y. *Science* **2011**, *334*, 1383-1385.

(18) Nie, Y.; Li, L.; Wei, Z. *Chem. Soc. Rev.* **2015**, *44*, 2168-2201.

(19) Petrie, J. R.; Cooper, V. R.; Freeland, J. W.; Meyer, T. L.; Zhang, Z.; Lutterman, D. A.; Lee, H. N. *J. Am. Chem. Soc.* **2016**, *138*, 2488-2491.

(20) Bockris, J. O. M.; Otagawa, T. *J. Electrochem. Soc.* **1984**, *131*, 290-302.

(21) Pesquera, D.; Herranz, G.; Barla, A.; Pellegrin, E.; Bondino, F.; Magnano, E.; Sánchez, F.; Fontcuberta, J. *Nat. Commun.* **2012**, *3*, 1189.

(22) Tung, I.; Balachandran, P.; Liu, J.; Gray, B.; Karapetrova, E.; Lee, J.; Chakhalian, J.; Bedzyk, M.; Rondinelli, J.; Freeland, J. *Phys. Rev. B* **2013**, *88*, 205112.

(23) Gupta, S.; Kellogg, W.; Xu, H.; Liu, X.; Cho, J.; Wu, G. *Chem Asian J* **2016**, *11*, 10-21.

(24) Akhade, S. A.; Kitchin, J. R. *J. Chem. Phys.* **2011**, *135*, 104702.

(25) Akhade, S. A.; Kitchin, J. R. *J. Chem. Phys.* **2012**, *137*, 084703.

(26) Yildiz, B. *MRS Bull.* **2014**, *39*, 147-156.

(27) Stoerzinger, K. A.; Choi, W. S.; Jeen, H.; Lee, H. N.; Shao-Horn, Y. *J. Phys. Chem. Lett.* **2015**, *6*, 487-492.

(28) Petrie, J. R.; Jeen, H.; Barron, S. C.; Meyer, T. L.; Lee, H. N. *J. Am. Chem. Soc.* **2016**.

(29) Misra, D.; Kundu, T. *J. Electron. Mater.* **2017**, *46*, 150-157.

(30) Koper, M. T. *J. Electroanal. Chem.* **2011**, *660*, 254-260.

(31) Rossmeisl, J.; Logadottir, A.; Nørskov, J. K. *Chem. Phys.* **2005**, *319*, 178-184.

(32) Rossmeisl, J.; Qu, Z.-W.; Zhu, H.; Kroes, G.-J.; Nørskov, J. K. *J. Electroanal. Chem.* **2007**, *607*, 83-89.

(33) Man, I. C.; Su, H.-Y.; Calle-Vallejo, F.; Hansen, H. A.; Martínez, J. I.; Inoglu, N. G.; Kitchin, J.; Jaramillo, T. F.; Nørskov, J. K.; Rossmeisl, J. *ChemCatChem* **2011**, *3*, 1159-1165.

(34) Tkalych, A. J.; Zhuang, H. L.; Carter, E. A. *ACS Catal.* **2017**, *7*, 5329-5339.

(35) Kresse, G.; Hafner, J. *Phys. Rev. B* **1993**, *47*, 558.

(36) Kresse, G.; Furthmüller, J. *Comput. Mater. Sci.* **1996**, *6*, 15-50.

(37) Kresse, G.; Furthmüller, J. *Phys. Rev. B* **1996**, *54*, 11169.

(38) Perdew, J. P.; Burke, K.; Ernzerhof, M. *Phys. Rev. Lett.* **1996**, *77*, 3865.

(39) Monkhorst, H. J.; Pack, J. D. *Phys. Rev. B* **1976**, *13*, 5188.

(40) Nocedal, J. *Math. Comput.* **1980**, *35*, 773-782.

(41) Kojima, T.; Nomura, K.; Miyazaki, Y.; Tanimoto, K. *J. Am. Ceram. Soc.* **2006**, *89*, 3610-3616.

(42) Nørskov, J. K.; Rossmeisl, J.; Logadottir, A.; Lindqvist, L.; Kitchin, J. R.; Bligaard, T.; Jonsson, H. *J. Phys. Chem. B* **2004**, *108*, 17886-17892.

(43) Valdes, A.; Qu, Z.; Kroes, G.; Rossmeisl, J.; Nørskov, J. K. *J. Phys. Chem. C* **2008**, *112*, 9872-9879.

(44) Hansen, H. A.; Rossmeisl, J.; Nørskov, J. K. *Phys. Chem. Chem. Phys.* **2008**, *10*, 3722-3730.

(45) Wang, Y.; Cheng, H.-P. *J. Phys. Chem. C* **2013**, *117*, 2106-2112.

(46) Li, M.; Zhang, L.; Xu, Q.; Niu, J.; Xia, Z. *J. Catal.* **2014**, *314*, 66-72.

(47) Hammer, B.; Norskov, J. *Nature* **1995**, *376*, 238.

(48) Hammer, B.; Nørskov, J. *Surf. Sci.* **1995**, *343*, 211-220.

(49) Hammer, B.; Morikawa, Y.; Nørskov, J. K. *Phys. Rev. Lett.* **1996**, *76*, 2141.

(50) Yourdshahyan, Y.; Cooper, V. R.; Kolpak, A. M.; Rappe, A. M. *Proc. SPIE* **2003**, *5223*, 223-232.

(51) Cooper, V. R.; Kolpak, A. M.; Yourdshahyan, Y.; Rappe, A. M. *Phys. Rev. B* **2005**, *72*, 081409.

(52) Lima, F.; Zhang, J.; Shao, M.; Sasaki, K.; Vukmirovic, M.; Ticianelli, E.; Adzic, R. *J. Phys. Chem. C* **2007**, *111*, 404-410.

(53) Mason, S. E.; Grinberg, I.; Rappe, A. M. *J. Phys. Chem. C* **2008**, *112*, 1963-1966.

(54) Yuk, S. F.; Asthagiri, A. *J. Chem. Phys.* **2015**, *142*, 124704.

(55) Tang, Q.-L.; Duan, X.-X.; Liu, B.; Wei, A.-Q.; Liu, S.-L.; Wang, Q.; Liang, Y.-P.; Ma, X.-H. *Appl. Surf. Sci.* **2016**, *363*, 128-139.
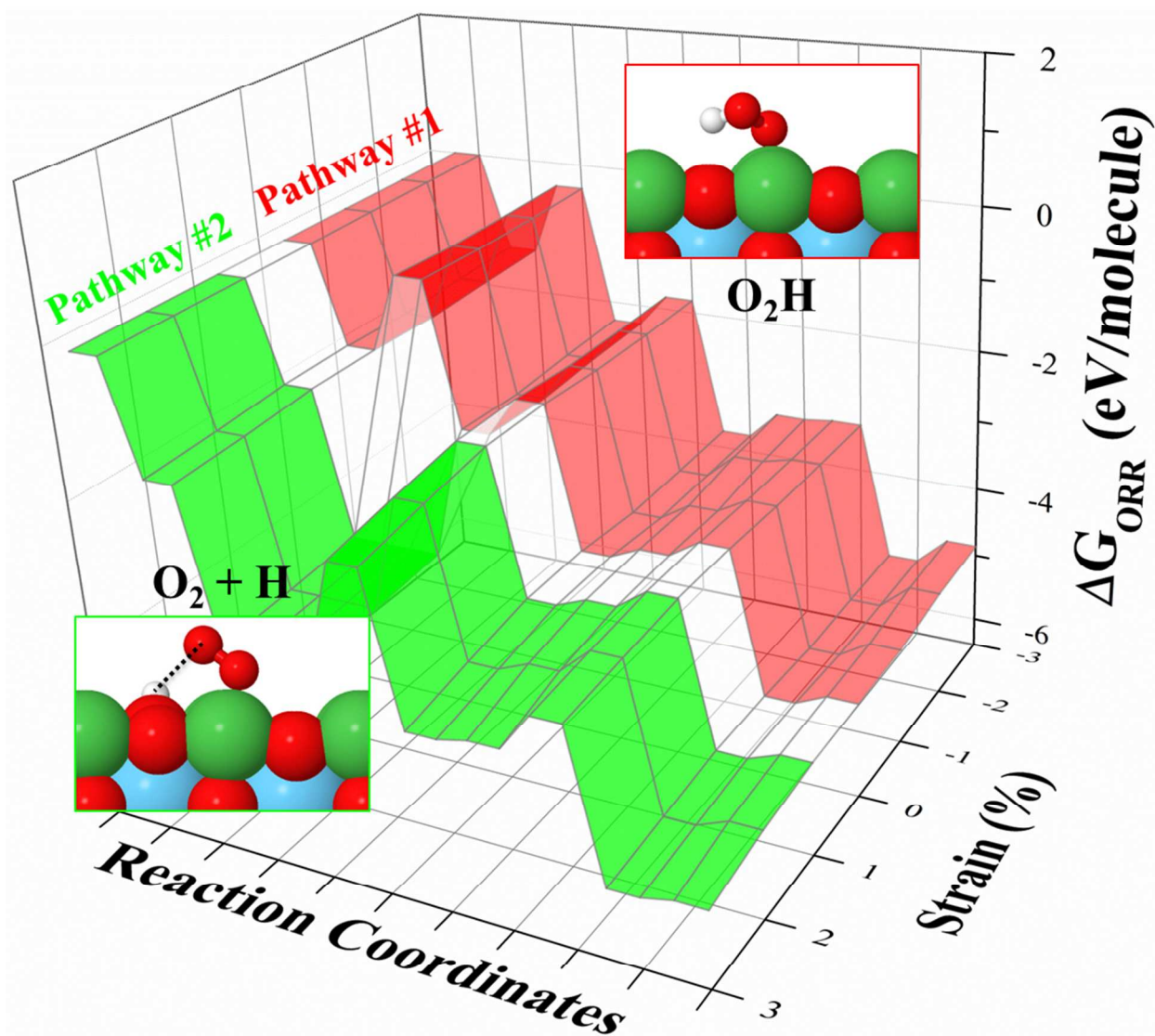
Theoretical insights into the influences of strain on the mechanisms of the oxygen evolution and oxygen reduction reactions on LaNiO$_3$(001).